Visualization of pinholin lesions in vivo

Ting Pang[a,1], Tinya C. Fleming[b], Kit Pogliano[b], and Ry Young[a,2]

[a]Center for Phage Technology, Department of Biochemistry and Biophysics, Texas A&M University, College Station, TX 77843-2128; and [b]Division of Biological Sciences, University of California at San Diego, La Jolla, CA 92093

Edited by Sankar Adhya, National Institutes of Health, National Cancer Institute, Bethesda, MD, and approved March 27, 2013 (received for review January 10, 2013)

Lambdoid phage 21 uses a pinholin–signal anchor release endolysin strategy to effect temporally regulated host lysis. In this strategy, the pinholin $S^{21}68$ accumulates harmlessly in the bilayer until suddenly triggering to form lethal membrane lesions, consisting of $S^{21}68$ heptamers with central pores <2 nm in diameter. The membrane depolarization caused by these pores activates the muralytic endolysin, R^{21}, leading immediately to peptidoglycan degradation. The lethal $S^{21}68$ complexes have been designated as pinholes to distinguish from the micrometer-scale holes formed by canonical holins. Here, we used GFP fusions of WT and mutant forms of $S^{21}68$ to show that the holin accumulates uniformly throughout the membrane until the time of triggering, when it suddenly redistributes into numerous small foci (rafts). Raft formation correlates with the depletion of the proton motive force, which is indicated by the potential-sensitive dye bis-(1,3-dibutylbarbituric acid)pentamethine oxonol. By contrast, GFP fusions of either antiholin variant $irsS^{21}68$, which only forms inactive dimers, or nonlethal mutant $S^{21}68_{S44C}$, which is blocked at an activated dimer stage of the pinhole formation pathway, were both blocked in a state of uniform distribution. In addition, fluorescence recovery after photobleaching revealed that, although the antiholin $irsS^{21}68$-GFP fusion was highly mobile in the membrane (even when the proton motive force was depleted), more than one-half of the $S^{21}68$-GFP molecules were immobile, and the rest were in mobile states with a much lower diffusion rate than the rate of $irsS^{21}68$-GFP. These results suggest a model in which, after transiting into an oligomeric state, $S^{21}68$ migrates into rafts with heterogeneous sizes, within which the final pinholes form.

bacteriophage | membrane protein | membrane potential | structured illumination microscopy

In general, the phage infection cycle is terminated by the function of the holin, a small viral membrane protein (1). Throughout the morphogenesis period, holins accumulate harmlessly in the cytoplasmic membrane until suddenly forming lethal membrane lesions (holes). This event, called triggering, occurs at an allele-specific time. The lesions formed by canonical holins are very large, with diameters of micrometer-scale, allowing the escape of prefolded phage endolysins from the cytoplasm (2, 3). However, another important class of holins, the pinholins, form holes too small for the passage of protein. The results of a combined biochemical, genetic, ultrastructural, and computational approach indicate that the prototype pinholin, $S^{21}68$ (Fig. 1 *A* and *B*), of lambdoid phage 21 of *Escherichia coli* forms heptamers with a central lumen <2 nm in diameter (4), too small to allow the passage of endolysin (5). Phages using pinholins, therefore, require a distinct class of muralytic enzymes called the signal anchor release (SAR) endolysins, which are exported in a membrane-tethered enzymatically inactive form during the latent period. When the pinholins trigger, the membrane is depolarized, resulting in the release of the SAR endolysin from the bilayer into the periplasm, where it refolds to a muralytically active form and attacks the peptidoglycan.

Investigation of the mechanism behind the scheduling of holin triggering and thus, the timing of the phage infection cycle has been limited to physiological and genetic studies. Triggering can be caused prematurely by even partial depolarization of the membrane with energy poisons or the imposition of anoxia on aerobic cultures. Moreover, the triggering time is highly sensitive to missense changes throughout holin sequences, especially in the transmembrane domains (TMDs) (6–9). Recently, real-time deconvolution fluorescence microscopic studies of a GFP-tagged version of S105, the canonical holin of phage λ, revealed that, irrespective of whether triggering occurred naturally or was induced by an energy poison, triggering could be correlated with the sudden shift from a state of uniform distribution in the inner membrane to the formation of large 2D aggregates or rafts (10). Although the structural relationship of these rafts to the enormous holes formed by S105 has not been established, the transition from the uniformly distributed state to the raft state has been equated with the holin attaining a critical concentration for nucleation, analogous to the transition observed for bacteriorhodopsin in the formation of the purple membrane arrays (11, 12).

Despite this conceptual advance, which offered a simple molecular basis for the timing function of holins, it remained unclear whether a similar mechanism would underlie the timing function of pinholins, because the formation of heptameric pinholes would not obviously require the formation of large rafts. The pinholin has two TMDs (Fig. 1 *B* and *C*). TMD1 is an intrinsic inhibitory domain that binds TMD2 and blocks it from proceeding to pinhole formation (7). Several lines of evidence indicate that the pinholin accumulates initially in inactive dimers (ID1s), with the TMD1 of each monomer interacting with TMD2 both *in cis* and *in trans* (Fig. 1*D*). Remarkably, TMD1 has been shown to be an SAR domain that exits the bilayer in a potential-sensitive manner (13) (Fig. 1*C*). To proceed down the pinhole formation pathway, both TMD1s in the inactive dimer must be externalized. The S^{21} gene actually encodes two proteins, the holin $S^{21}68$ and a longer product $S^{21}71$, which because it has a basic residue among its additional three N-terminal amino acids (Met1-Lys2-Ser3), exhibits retarded externalization of TMD1 (Fig. 1 *A* and *C*); *in trans*, it retards the triggering of

Significance

How a virus schedules the termination of its infection cycle is a mystery. Here, we show that a small-membrane protein called a pinholin controls the infection cycle of a bacterial virus. By tagging the pinholin with a fluorescent marker, we show that, while the virus is replicating, the pinholin accumulates harmlessly and uniformly in the membrane until suddenly aggregating into foci (rafts), causing a fatal deenergization of the bacterial membrane and the onset of lysis. The entire temporal program of the virus may, thus, depend on achieving a critical concentration of a single protein.

Author contributions: T.P., T.C.F., K.P., and R.Y. designed research; T.P. and T.C.F. performed research; K.P. contributed new reagents/analytic tools; T.P., T.C.F., K.P., and R.Y. analyzed data; and T.P., T.C.F., K.P., and R.Y. wrote the paper.

The authors declare no conflict of interest.

This article is a PNAS Direct Submission.

[1]Present address: Department of Microbiology and Immunobiology, Harvard Medical School, Boston, MA 02115.

[2]To whom correspondence should be addressed. E-mail: ryland@tamu.edu.

This article contains supporting information online at www.pnas.org/lookup/suppl/doi:10.1073/pnas.1222283110/-/DCSupplemental.

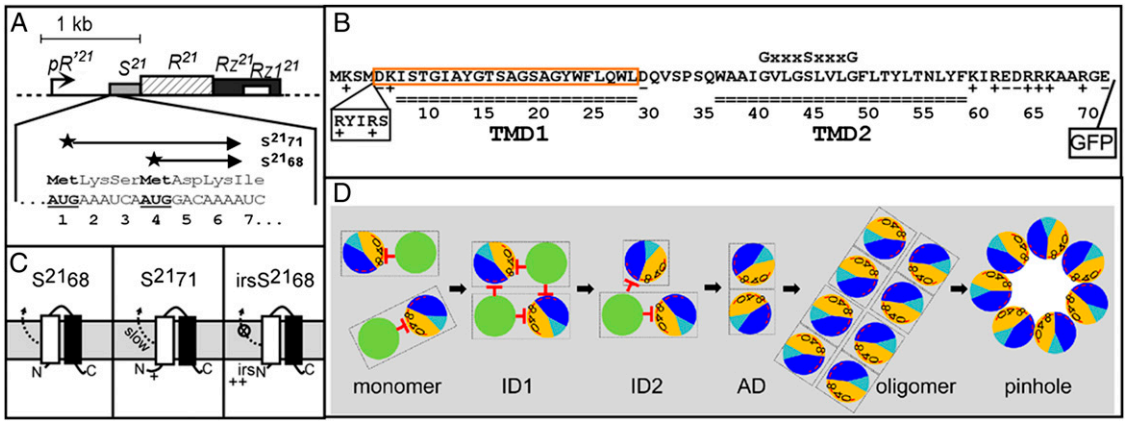

Fig. 1. Features of the phage 21 holin S^{21}. (*A*) Phage 21 lysis cassette. The phage 21 lysis genes *S*, *R*, *Rz*, and *Rz1* are located downstream of the late gene promoter pR'^{21}. The S^{21} gene has a dual-start motif, encoding both the holin $S^{21}68$ and the antiholin $S^{21}71$ (13, 14). Both start codons are bold and underlined. Reproduced from ref. 7 with permission of John Wiley & Sons, Inc. Copyright 2010 Blackwell Publishing Ltd. (*B*) The primary structure of S^{21}. The S^{21} reading frame is shown, with TMD1 and TMD2 indicated by the double underscore. The residues deleted in $S^{21}68_{\Delta TMD1}$ are boxed in orange. The position and sequence of the *irs* epitope in $irsS^{21}68$ are shown in a box below the sequence. The codons encoding the linker residues Pro-Gly followed by *gfp* are inserted at the extreme C terminus and shown as a boxed GFP. The glycine zipper motif is shown over positions 40–48. (*C*) The membrane topology of $S^{21}68$ (*Left*), $S^{21}71$ (*Center*), and $irsS^{21}68$ (*Right*). White box, TMD1; black box, TMD2. The TMD1 of $S^{21}68$ is initially inserted in the membrane but later released into the periplasm (13) (*D*). The externalization of TMD1 is delayed in the context of $S^{21}71$ and completely blocked in the context of $irsS^{21}68$ (*B*). Reproduced from ref. 7 with permission of John Wiley & Sons, Inc. Copyright 2010 Blackwell Publishing Ltd. (*D*) Model of S^{21} hole formation pathway (top-down view from periplasm). The two TMDs (green, TMD1; sectored, TMD2) in a single S^{21} molecule are boxed. TMD2 contains two interacting faces, A and B, represented by orange and dark blue, respectively (*4*); 0, 4, and 8 indicate the helical positions of G40, S44, and G48, respectively. Red arc, hydrophilic and weakly hydrophobic residues in TMD2. After being inserted in the membrane as a monomer, $S^{21}68$ and $S^{21}71$ molecules form IDs (ID1), with TMD1 inhibiting TMD2 both *in cis* and *in trans*, represented by red stop arrows. A second ID (ID2) state may form for ID1 formed between $S^{21}68$ and $S^{21}71$, with only the TMD1 of $S^{21}68$ released from the membrane. The release of both TMD1s results in the formation of the activated dimer (AD) form, involving a homotypic helix–helix interaction through interface A, which contains the glycine zipper motif. This intermediate state is proposed to proceed to an oligomeric state, in which A:B interhelix interactions dominate. Finally, in a transition probably driven by hydration of the luminal residues, the lethal heptameric pinholes form with exclusively A:B interactions. Reproduced from ref. 15 with permission of John Wiley & Sons, Inc. Copyright 2010 Blackwell Publishing Ltd.

$S^{21}68$ (13, 14). $S^{21}71$ is, thus, an antiholin, albeit a weak one, because it is a specific inhibitor of the holin form $S^{21}68$. Dominant-negative antiholin character is even more pronounced with the constructed allele *irsS21-68*, which has the IRS epitope (sequence RYIRS), with two positive charges, at the N terminus of $S^{21}68$ (Fig. 1 *B* and *C*). Because TMD1 of $irsS^{21}68$ is locked in the bilayer, the protein has an absolute triggering defect and also blocks $S^{21}68$ function by forming inactive heterodimers with it (13). Using this strong antiholin construct, it has been shown that both TMD1s have to be externalized to allow oligomerization of the pinholin. Although the presence of the externalized TMD1 domains facilitates hole formation, a derivative lacking TMD1 entirely, $S^{21}68_{\Delta TMD1}$, is fully active and exhibits temporally scheduled triggering, indicating that the topological dynamics of TMD1 serve as a gate-keeping switch that allows entry of the pinholin molecules into the triggering pathway (13, 15). Other mutants, like $S^{21}68_{S44C}$, have been isolated that block pinhole formation in activated dimer states farther downstream in the pathway. The final product of the pathway at the triggering time is, under physiological levels of expression, up to ~900 heptameric pinholes. Computational and biochemical studies identified two interacting surfaces of TMD2 (A and B), with surface A containing a glycine zipper motif, $G_{40}xxxS_{44}xxxG_{48}$, shown to be important in helix–helix interactions (16, 17) (Fig. 1 *B* and *D*). In the current model, the early dimer states of the pinholin are defined by homotypic A:A interactions, with a transition to heterotypic A:B interactions developing during later oligomeric states.

The pathway to triggering and hole formation is, thus, much better understood for the pinholin than for the canonical λ holin. Nevertheless, as with canonical holins, the mechanism of triggering and the molecular basis of the allele-specific timing are unknown. For canonical holins, the simplest notion is that the holin rafts are incompatible with maintaining the membrane potential, possibly because the intimate interhelical packing may deplete the raft of lipids and create ion leakiness. Thus, formation of the first raft or raft subdomain would lead to at least local depolarization, which would then lead to the formation of more extensive rafts and depolarization throughout the membrane. A prediction of this scheme is that, because pinholins exhibit the same proton motive force (PMF) -dependent triggering phenotype, rafts would also be formed in the pinhole pathway, although high-level oligomerization would not necessarily be required for the formation of heptameric structures. Here, we use GFP fusions, real-time fluorescence deconvolution microscopy, and superresolution microscopy to test this prediction. The results are discussed in terms of the current model for the pinholin pathway to lysis.

Results

GFP Tag Does Not Affect the Function of $S^{21}68$ or Its Variants. To observe the localization of $S^{21}68$ and its variants, GFP was fused to the C terminus of each protein with a Pro-Gly linker (Fig. 1*B*). The $S^{21}68$-GFP fusion retained holin function, which was judged by the abrupt cessation of culture growth, indicative of triggering to pinhole formation and the resulting PMF depletion (Fig. 2 *A* and *B*) (13). Similarly, the GFP fusions of the truncated pinholin $S^{21}68_{\Delta TMD1}$ and the lytic mutant $S^{21}68_{V46C}$ also exhibited lethal function. Finally, nonlethal phenotypes of the antiholin $irsS^{21}68$ and the nonlytic mutant $S^{21}68_{S44C}$ were retained: neither protein supported lethal triggering, even after depolarization of the membrane by treatment with the uncoupler 2,4-dinitrophenol (DNP) (Fig. 2*B*). Although there were variations in protein expression, all of the chimeric proteins localized to the insoluble fraction containing the membrane (Fig. 2 *C* and *D*). Comparison of the $S^{21}68$-GFP accumulation level with purified protein revealed that ~10^4 $S^{21}68$-GFP molecules were present at the time of triggering (Fig. 2*E*); this level is approximately the same as the level observed for the WT $S^{21}68$ pinholin (~6.5×10^3) (4)

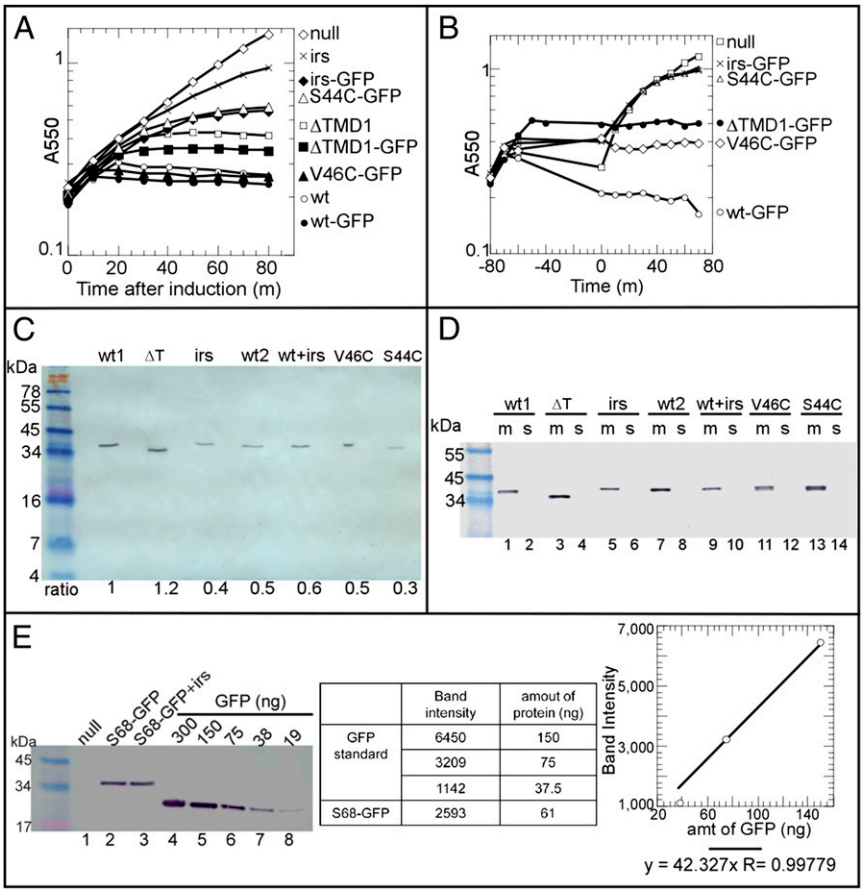

Fig. 2. Holin function is preserved in the presence of the C-terminal GFP tag. (*A*) Triggering phenotypes of *S*^{21}*68-gfp* alleles. Cultures were induced at *t* = 0 and monitored for growth. The cells carried two plasmids: pQ, which supplies the Q late gene activator under IPTG-inducible control, and isogenic variants of the expression vector pRE, in which different *S*^{21}*68* alleles or *S*^{21}*68-gfp* fusion alleles are under control of the λ-late promoter pR′ (Table 2). Open diamonds, pRE; open circles, pR′S^{21}68; open squares, pS^{21}68$_{\Delta TMD1}$; ×, pirsS^{21}68; closed circles, pS^{21}68^{GFP}; closed squares, pS^{21}68$_{\Delta TMD1}$^{GFP}; closed diamonds, pirsS^{21}68^{GFP}; open triangles, pS^{21}68^{GFP}$_{S44C}$; closed triangles, pS^{21}68^{GFP}$_{V46C}$. (*B*) Triggering induced with the uncoupler DNP. Cultures expressing S^{21}68-GFP (open circles), S^{21}68$_{\Delta TMD1}$-GFP (closed circles), S^{21}68$_{S44C}$-GFP (open triangles), S^{21}68$_{V46C}$-GFP (open diamonds), irsS^{21}68-GFP (×), or the negative control (open squares) were induced at *t* = −80 min. DNP was added at a final concentration of 2 mM to each culture at *t* = −70 min (the time when WT triggers) or *t* = −50 min for S^{21}68$_{\Delta TMD1}$-GFP, which is its triggering time; 10 min after the addition of DNP, cells were collected by centrifugation, washed, and resuspended in fresh LB media. At *t* = 0, growth of each culture was monitored again. (*C*) Protein accumulation level of the *S*^{21}*68-gfp* alleles. Cultures producing the indicated protein were induced and sampled into TCA. Sampling time varied with the allele. For lethal alleles, samples were taken at the triggering time. For mutant nonlethal alleles, samples were taken at the time of WT triggering (10 m). The culture expressing *irsS*^{21}*68-gfp* was sampled at 30 min. wt1/ wt2, S^{21}68-GFP; ΔT, S^{21}68$_{\Delta TMD1}$-GFP; irs, irsS^{21}68-GFP; wt+irs, S^{21}68-GFP with the presence of irsS^{21}68; V46C, S^{21}68 $_{V46C}$-GFP; S44C, S^{21}68 $_{S44C}$-GFP. Wt1 was expressed from a strain carrying plasmids pQ and pR′S^{21}68. Samples labeled as wt2 and wt+irs were from cultures carrying the prophage λ*cam*(*S68-gfpR*$_{am}$*RzRz1*)^{21} and plasmid pRE (wt2) or pirsS^{21}68 (wt+irs), respectively. Western blotting was performed using antibodies against GFP. The relative protein accumulation level normalized to the parental S^{21}68-GFP level is indicated at the bottom of each lane. (*D*) Membrane fractionation of S^{21}68-GFP and its variants. Cultures were harvested as in *C*, except that samples were fractionated into membrane (m) and soluble (s) samples. (*E*) Measurement of S^{21}68-GFP expression level at the time of triggering. Cultures were thermally induced, and an aliquot of 1.5 × 10^8 cells was precipitated by TCA immediately after S^{21}68-GFP triggering. Samples were subjected to SDS/PAGE and Western blotting in parallel with samples containing a known amount of purified GFP. (*Left*) Lane 1, MDS12*tonA::Tn10*[λ*cam*Δ(*SR*)]; lanes 2 and 3, MDS12*tonA::Tn10*[λ*cam*(*S68-gfpR*$_{am}$*RzRz1*)^{21}] carrying plasmid pRE or pirsS^{21}68, respectively; lanes 4–8, purified GFP in the amount indicated. The band intensities, measured using ImageJ software (31), are (*Center*) listed in the table and (*Right*) analyzed in the plot, yielding 60 ng S^{21}68-GFP accumulated in 1.5 × 10^8 cells. On this basis, ∼9,000 S^{21}68-GFP molecules were present at the triggering time.

within the precision available for estimating protein concentrations by Coomassie blue staining. Overall, the addition of GFP as a C-terminal cytoplasmic tag had no deleterious effect on the function of S^{21}68 or its variants.

Pinholins Trigger to Form Small Rafts in the Membrane. The localization of GFP-fused pinholins after triggering was observed by deconvolution fluorescence microscopy (Fig. 3*A*). All of the functional pinholins, S^{21}68, S^{21}68$_{V46C}$, and S^{21}68$_{\Delta TMD1}$, were found to form numerous small patches. To be consistent with the terminology used for the S105-GFP studies, these foci were designated as pinholin rafts (10). In contrast, the inactive antiholin irsS^{21}68 and the nonlethal mutant S^{21}68$_{S44C}$ both remained evenly distributed in the membrane. Previous results have shown that both species are limited to the formation of dimers (15). To test if the formation of patches was an artifact of membrane depolarization, the uncoupler DNP was added to the induced cultures before harvesting for the fluorescence microscopy. The addition of DNP had no detectable effect on the distribution of either protein (Fig. 3*A*). Thus, formation of the rafts correlates specifically with lethal pinhole formation.

We next performed superresolution imaging of GFP fluorescence with the various pinholin fusion proteins using the DeltaVision OMX Microscope (Applied Precision), which uses 3D structured illumination microscopy to achieve up to 100 nm resolution. Distinct small rafts were observed for S^{21}68 but not for

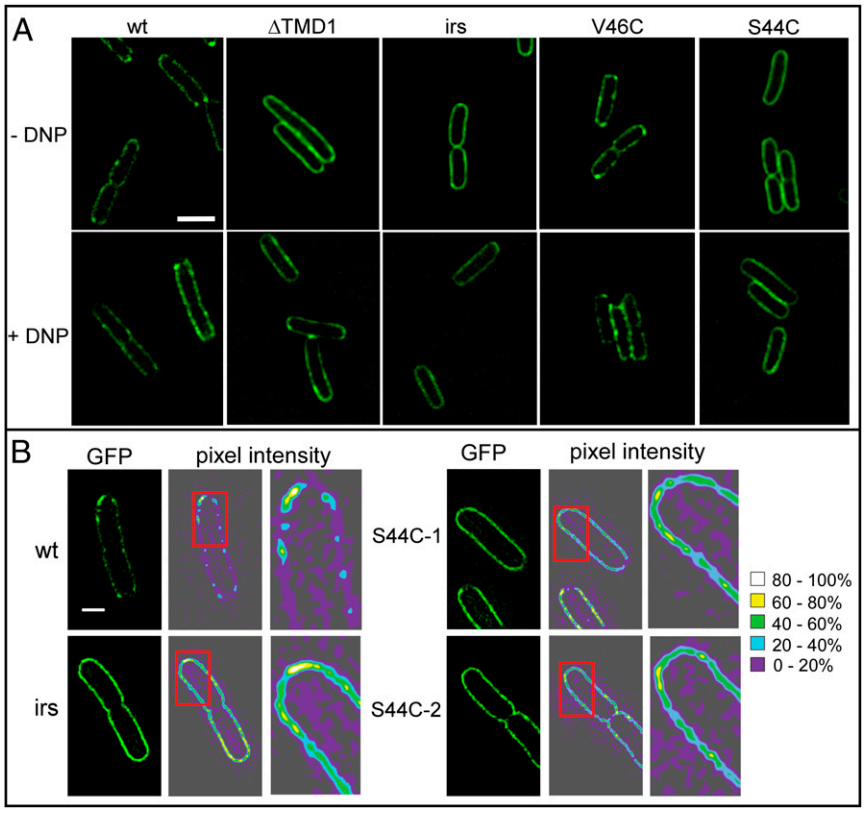

Fig. 3. Raft formation by the pinholin $S^{21}68$-GFP. Cultures of *E. coli* cells expressing the GFP fusions corresponding to $S^{21}68$ alleles indicated above the micrographs were induced, harvested at the time of pinholin triggering, and prepared for microscopy. For the nontriggering alleles, $irsS^{21}68$ (irs), and $S^{21}68_{S44C}$ (S44C), harvesting was done at 30 or 10 min, respectively. (*A*) Deconvolution fluorescence imaging of cultures expressing $S^{21}68$-GFP and its variants. Samples were mixed with membrane dye FM4-64 and placed onto agarose pads. Images were captured for 10 Z sections 0.2 μm apart for each sample. Shown are images taken at the midfocal plane. Samples in *Lower* were treated with 2 mM DNP for 10 min before harvesting. (Scale bar: 2 μm.) (*B*) Superresolution image (GFP) and pixel intensity maps (pixel intensity). Samples were prepared as for *A*. Fluorescent images were obtained using structured illumination microscopy to provide a resolution of 100 nm. Pixel intensity maps of GFP fluorescence were scaled so that the maximum value is 100% and that 0% represents 2 SDs above the average background value. Purple, 0–20%; blue, 20–40%; green, 40–60%; yellow, 60–80%; white, 80–100%. Columns 3 and 6 are zoomed-in views of the regions in the red boxes in columns 2 and 5.

nonlethal fusions (both the antiholin $irsS^{21}68$ and the missense mutant $S^{21}68_{S44C}$) (Fig. 3*B*). The GFP fluorescence was quantified for the lethal $S^{21}68$ and nonlethal $irsS^{21}68$ fusion alleles (Fig. S1 and Table S1) from 31 cells in each case. For the former, fluorescence was concentrated into an average of 16 rafts per cell, averaging 0.01 μm^2 in area. In contrast, the fluorescence in the $irsS^{21}68$ inductions was present in domains spanning a wide range of sizes, mostly greater than 0.3 μm^2, indicating that the GFP-tagged protein is widely dispersed throughout the membrane. In these cells, cells with even fluorescence throughout the whole membrane have a fluorescent region of about 1 μm^2 (area of cell outline). Those cells usually had only one fluorescent region.

Antiholin Inhibits the Formation of Rafts. The antiholin $irsS^{21}68$ not only inhibits the pinholin function of $S^{21}68$ but also blocks its oligomerization by forming heterodimers (4, 13). We, therefore, addressed whether $irsS^{21}68$ would inhibit raft formation by the WT fusion. To this end, a lysogen was constructed with the $S^{21}68$-*gfp* allele on the prophage and $irsS^{21}68$ *in trans* under the native late promoter on a medium copy plasmid, $pirsS^{21}68$. The expression of $irsS^{21}68$ had no effect on the accumulation of $S^{21}68$-GFP protein (Fig. 2*C*), but it completely inhibited its function (Fig. 4*A*) and raft formation (Fig. 4 *B* and *C*). Moreover, when the antiholin function of $irsS^{21}68$ is subverted by the addition of DNP, triggering and raft formation are observed. Thus, in every case, raft formation is correlated with the lethal function of the pinholin, strongly suggesting that raft formation is required for formation of the pinholes.

Pinhole Formation Depletes the PMF. Previously, the dissipation of the PMF caused by pinhole formation was monitored by following growth of induced batch cultures (5, 7). To correlate membrane depolarization with raft formation directly, the potential-sensitive fluorescent probe bis-(1,3-dibutylbarbituric acid) pentamethine oxonol [DiBAC4(5)] was added to cultures expressing pinholin $S^{21}68$-GFP or its variants. DiBAC4(5) is a lipid-soluble anionic dye that partitions across depolarized but not polarized membranes (18); therefore, it preferentially stains depolarized cells. As expected, staining was observed with cells expressing functional pinholin fusions, $S^{21}68$-GFP and $S^{21}68_{V46C}$-GFP, but not nonfunctional variants, like $S^{21}68_{S44C}$-GFP or the antiholin $irsS^{21}68$-GFP, indicating that raft formation leads to depletion of the PMF (Fig. 5*A*). To correlate the time of raft formation to the depletion of PMF, cells carrying plasmids expressing $S^{21}68$-GFP were grown on agarose pads containing DiBAC4(5). Fluorescent images were taken every 1 min after the induction of protein expression. Multiple stable rafts appeared at the same time that DiBAC4(5) began to stain the cell and reached full staining ~3 min later (Fig. 5 *B* and *C*). This result shows that the formation of $S^{21}68$-GFP rafts is associated with rapid depletion of the PMF and consistent with the abrupt cessation of growth observed at allele-specific times after induction of pinholin expression in batch cultures (7).

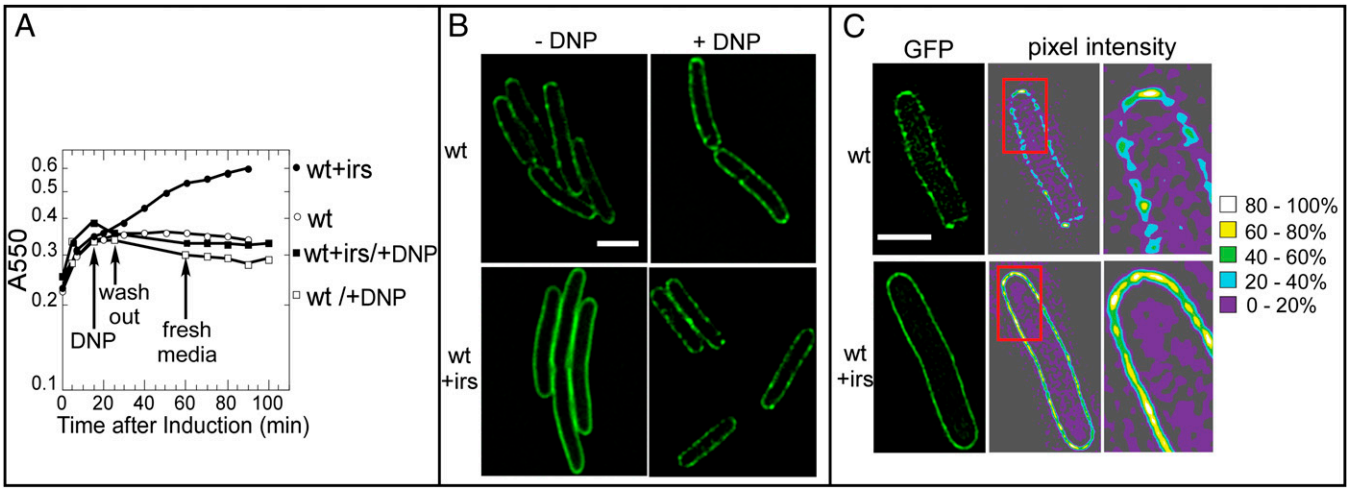

Fig. 4. The antiholin irsS^{21}68 inhibits both the triggering and raft formation of S^{21}68-GFP. (*A*) irsS^{21}68 inhibits the triggering of S^{21}68-GFP. Expression of S^{21}68-GFP alone (open symbols, wt) or with irsS^{21}68 expressed *in trans* (filled symbols, wt+irs) was thermally induced in the lysogen MDS12Δ*tonA*[λ*cam* (*S68-gfpR*$_{am}$*RzRz1*)^{21}] carrying the vector pRE or pirsS^{21}68, respectively. After thermally induced at t = 0, growth of each culture was monitored as A550. Circles indicate culture not being treated with DNP. Squares indicate culture treated with 2 mM DNP at 20 min after induction. DNP was washed out 10 min later and replaced with fresh LB media. Culture growth was monitored again at 60 min after induction. (*B*) irsS^{21}68 inhibits the raft formation of S^{21}68-GFP. Cultures in *A* were harvested at 20 min after induction. Fluorescent images of each sample were taken as in Fig. 3*A*. (*C*) Superresolution image (*Left*) and map of S^{21}68-GFP intensity (*Center* and *Right*). Samples were prepared, and fluorescent images were taken and analyzed as in Fig. 3*B*. *Upper* show formation of S^{21}68-GFP (wt) rafts, which are absent (*Lower*) when irsS^{21}68 is coexpressed (wt+irs).

Fluorescence Recovery After Photobleaching Evidence for Multiple Mobility States of the Pinholin. We next used fluorescence recovery after photobleaching (FRAP) assays to assess the mobility of the S^{21}68-GFP chimera in the membrane. The antiholin construct, irsS^{21}68-GFP, was found to be fully mobile, with a half-time of recovery ($t_{1/2}$) of ~6 s (Fig. 6 *A* and *E* and Table 1), consistent with its existence as ID1 (Fig. 1*D*) in vivo (4). Moreover, this mobility was unaffected by the addition of DNP to collapse the PMF (Fig. 6*D*). By contrast, when the WT pinholin S^{21}68-GFP is photobleached, the fluorescence recovered to only ~47% of a nonbleached region (Fig. 6 *B* and *E* and Table 1), indicating that approximately one-half the protein is immobile. Moreover, the mobile fraction showed relatively long recovery times, with $t_{1/2}$ ~ 50 s. Given the relative size of the heptameric pinhole to the inactive dimer and the unpredictable effect of the seven TMD1s that are removed from the membrane and deployed to the periplasm, the simplest interpretation is that, after triggering, about one-half of the pinholes are clustered in immobile rafts, and the other one-half may be diffusing at a much slower rate than inactive dimers within the membrane. As expected, the presence of the antiholin irsS^{21}68 *in trans* allowed complete fluorescence recovery of S^{21}68-GFP, consistent with the antiholin keeping the holin-GFP molecules in the mobile inactive dimer state (Fig. 6 *C* and *E*). Interestingly, although 100% of the population is mobile (indicated by complete fluorescence recovery), the recovery time of the irsS^{21}68/S^{21}68-GFP complexes is slightly longer than the recovery time of irsS^{21}68-GFP but still much shorter than S^{21}68-GFP (Table 1). This slightly longer recovery time may indicate that, in the former, the TMD1s of many of the S^{21}68-GFP molecules in the inactive heterodimers have exited the membrane and may be supporting homotypic interactions in the periplasm, leading higher-order inactive complexes that move slower.

Discussion

Unified Model for Holin and Pinholin Timing. Although holins are extremely diverse in primary structure and membrane topology and come in two functionally distinct types, the canonical holins and the pinholins, they have three common functional features (19). First, many minutes after the onset of expression at the beginning of the morphogenesis phase of the infection cycle, holins suddenly trigger to halt respiration and macromolecular synthesis, depolarize the membrane, and kill the cell, irrespective of the presence or function of the other proteins involved in phage lysis. Second, the spontaneous triggering time can be advanced or retarded dramatically by single missense changes, especially in the residues of TMDs. Third, triggering can be artificially imposed by treatment of the cells with any condition or chemical agent that causes even a marginal reduction in the PMF.

We have previously proposed a model for the triggering pathway of the prototype canonical holin, the λ-S105 protein, based on recent studies with S105-GFP fusion proteins as well as multiple lines of evidence from the genetics, biochemistry, and physiology of the lysis process (10). The central theme of this model is that the lethal triggering event corresponds to the sudden transition of the holin molecules from a population of mobile dimers uniformly dispersed in the membrane to a few large foci or rafts, which then reorganize into extremely large, nonspecific holes. Although molecular details are still lacking, the general model provides for a conceptual framework for addressing the two fundamental questions about holins: what is the nature of the lethal hole, and how is the timing of holin function accomplished? A corollary to the model is that the sudden transition occurs when the concentration of the mobile dimers reaches an allele-specific critical concentration for nucleation of the rafts. Here, also using a GFP fusion approach, we have addressed whether this model can also apply to the prototype pinholin, S^{21}68, which instead of forming the large, nonspecific lesions of the canonical holin S105, forms regular heptameric pinholes incapable of allowing protein release.

To recapitulate the key findings here, we first showed that the fusion of GFP to the C terminus of the pinholin was not deleterious to its timing or lethal function, which was monitored by the sudden cessation of growth of the induced cells. Then, we showed that the pinholin–GFP fusions formed rafts, and just as for the S105 holin, raft formation was exclusively coupled with whether the S^{21} allele was lethal. The timing of raft formation was consistent with the triggering time within the limits of correlating liquid growth and growth on the microscopy slide. In

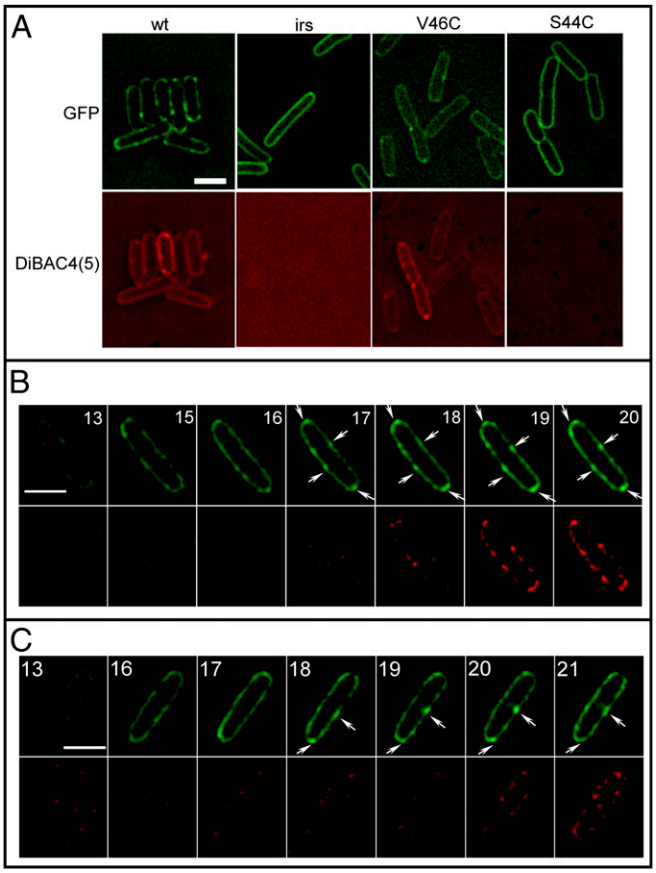

Fig. 5. Correlation between raft formation and PMF depletion. (*A*) Deconvolution fluorescent images of cells stained with the potential-sensitive dye DiBAC4(5). Samples from cells expressing the GFP fusions of the $S^{21}68$ variants indicated above the images were harvested at the same time as in Fig. 3 and stained with DiBAC4(5). (*Upper*) GFP fluorescence. (*Lower*) DiBAC4(5) fluorescence. The DiBAC4(5) fluorescence of each sample was adjusted to normalize the brightness relative to that of the WT. (Scale bar: 2 μm.) (*B* and *C*) Time-lapse images of cells expressing $S^{21}68$-GFP and stained with DiBAC4(5). Two representative cells are shown, with the time (in minutes) after induction indicated on each panel. Arrows indicate protein rafts. Green, GFP; red, DiBAC4(5). The brightness/contrast of all panels in *B* and *C* is adjusted individually based on the last time point. (Scale bar: 2 μm.)

addition, an antiholin product of the pinholin gene, expressed *in trans* to the pinholin–GFP fusion, was shown to block both $S^{21}68$-GFP lethality and raft formation. Finally, by using a potential-sensitive dye DiBAC4(5), we were able to correlate the formation of the rafts with the depletion of the PMF, again with timing consistent with the observed triggering time.

Taken together, these results support the notion that the model for triggering formulated for the canonical holin S105 also applies to the prototype pinholin $S^{21}68$ (Fig. 7). In both cases, triggering is explained as the result of the holin protein reaching a critical concentration, nucleating to form rafts, which then causes membrane depolarization, and as a result of this depolarization, reorganizing within these rafts to form the lethal holes. One only has to invoke that the conformational change induced by depolarization leads to heptameric pinhole formation within the pinholin aggregates instead of highly multimeric S105 wall assemblies [figure 6 in the work by White et al. (10)].

Differences Between the Holin and the Pinholin. One difference found here, compared with the S105-GFP system, was that the pinholin fusions formed rafts that were both smaller and more numerous per cell. Because these experiments have been done with only one canonical holin and one pinholin, respectively, it is not certain that these differences will be characteristic of either class. Nevertheless, it is worth noting that, after the exit of TMD1 from the bilayer, the $S^{21}68$ pinholin has only a single TMD with which to participate in the lateral interactions that must be required for raft formation, suggesting that the pinholins may accrete to the raft by simple symmetry-defined rules and that, for example, the tendency to leak protons might increase predictably with n-mer status. In contrast, S105 has three TMDs, linked by short sequences rich in Gly and Pro residues, which could generate significant complexity in the 2D helical packing of the S105 raft. This altered packing might allow much larger rafts to form before ion leakage leads to local depolarization. In addition, the behavior of purified $S^{21}68$ and S105 in the nonionic detergent dodecylmaltoside supports the notion that the canonical holin has much more scope for protein–protein interactions (20). S105 was found to form highly oligomeric ring structures estimated to contain >70 molecules, whereas $S^{21}68$ forms a heptameric homooligomer in dodecylmaltoside (4).

Of course, the final product of the pinholin triggering pathway is fundamentally different from the final product of the canonical holin pathway. The pinholin triggers to form $\sim 10^3$ heptameric pinholes, estimated to have channel diameters of ~2 nm; at the observed average of 16 rafts per cell, the typical raft is thus estimated to have ~60 heptameric pinholes within it. In contrast, the cryo-EM and tomography studies found that S105 formed one to three lesions averaging >300 nm in diameter per cell (3). Assuming that the S105 protein lines the walls of the holes, $>10^3$–3×10^3 molecules would be involved in holes in each cell, depending on how many of the three TMDs face the lumen and assuming ~1 nm wall perimeter per TMD (2, 3). In the S105-GFP studies, an average of three to four large S105-GFP rafts was observed, estimated to contain roughly $\sim 10^3$ holins, consistent with the number of holins needed to line the holes. A caveat for this perspective is that, for the S105 lesions, all that is known is the average diameter of the interruption in the bilayer, presumably proteinaceous, seen in the cross-section. The actual holes may be more like Swiss cheese, with multiple aqueous channels formed within the raft, in which case the total perimeter of the hole structure and thus, the number of holin molecules will be larger, scaling with the inverse of the average diameter of the component holes.

In any case, these considerations may also explain the phenotypic differences of the holin and pinholin GFP fusions. In the latter, the fusion of the GFP domain directly to the cytoplasmic C terminus of $S^{21}68$ had no deleterious effect on its capacity for lethal function, even to the details of timing. In contrast, to retain lethal function in the S105-GFP fusion protein, a 33-residue linker was required; shorter linkers abolished the ability of the chimera to trigger (10). Moreover, even with this large linker, the S105-GFP chimera exhibited greatly retarded triggering (95 vs. 45 min for S105 under these conditions), indicating that its critical concentration is much larger. This phenotypic difference may reflect the simpler structure of the heptameric pinhole, where the cytoplasmic C termini are predicted to be radially and symmetrically disposed, thus allowing the addition of the GFP tag without steric interference. In contrast, the micrometer-scale lesions formed by S105-GFP would require that the walls of the hole have little curvature per molecule compared with the nanometer scale of the TMDs that presumably line the walls. The presence of the bulky GFP tag could, under these circumstances, be expected to cause steric effects unfavorable for hole formation and be ameliorated only partially by the long linker.

Finally, another interesting difference is that the FRAP experiments indicated that a substantial fraction (47%) of the pinholin-GFP molecules is still mobile even after triggering, although with a lower mobility than the untriggered molecules. In contrast, nearly all of the triggered S105-GFP protein was found

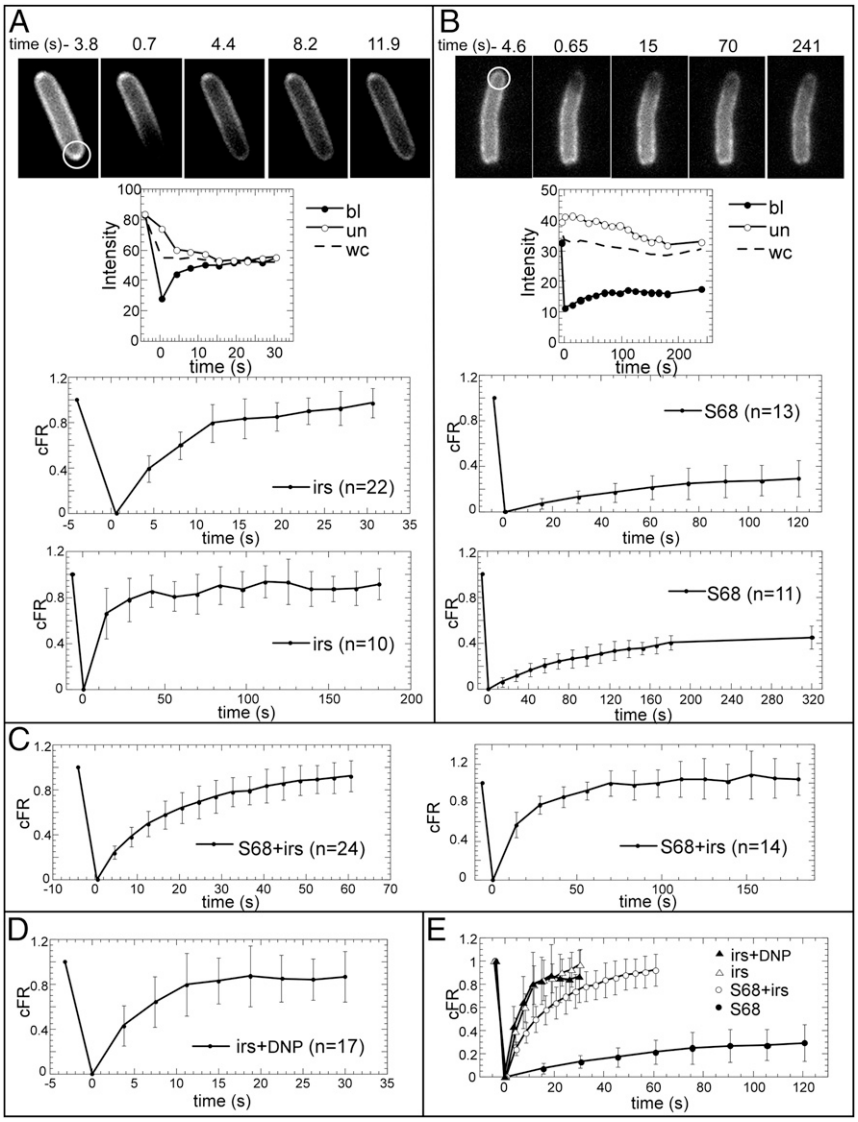

Fig. 6. Variation of the mobility between pinholin and antiholin. (*A* and *B*) FRAP analysis of antiholin irsS^{21}68-GFP (*A*) and pinholin S^{21}68-GFP (*B*). Cells expressing irsS^{21}68-GFP (*A*) or S^{21}68-GFP (*B*) were laser-bleached in the region indicated by the circle at $t = 0$. Subsequent GFP images were collected with 2.5-s exposures. In the representative intensity graph, GFP fluorescence intensities of the whole cell (wc; dashed line), bleached region (bl; filled circles), and unbleached region (un; open circles), with background fluorescence subtracted, are shown. The cFR was calculated for each sample as described in *Experimental Procedures* and plotted. Error bars indicate SD. *n* is number of cells individually photobleached and analyzed. (*C*) FRAP analysis of S^{21}68-GFP in the presence of irsS^{21}68. Same as *A*, except that cells were expressing irsS^{21}68 *in trans* to S^{21}68-GFP. (*D*) FRAP analysis of irsS^{21}68-GFP with the addition of DNP. Same as *A*, except that cells expressing irsS^{21}68-GFP were treated with 2 mM DNP for 10 min before sample collection and analysis. (*E*) Comparison of cFR. To compare the fluorescence recovery rate of each protein, cFR kinetics of the different GFP-tagged proteins were plotted together. Filled circles, S^{21}68-GFP ($n = 13$); open circles, S^{21}68-GFP in the presence of irsS^{21}68 ($n = 24$); open triangles, irsS^{21}68-GFP ($n = 22$); filled triangles, irsS^{21}68-GFP with the addition of DNP ($n = 17$).

to be immobilized, indicative of participation in highly oligomeric structures (10). The simplest interpretation is that the post-triggering mobile form is free heptameric pinholes. We suggest that the fact that ~50% of the pinholin-GFP is immobile reflects the origin of the pinholes within the original, large 2D rafts and that, at the edges of the triggered rafts, oligomerized pinholes are in equilibrium with free and mobile pinholes.

Perspective. It was already established that both holin and pinholins can be triggered by depolarization of the membrane to form lethal holes, and the results reported here establish that triggering is associated with raft formation. As noted above, the simplest notion is that raft formation causes depolarization and that depolarization in the context of the raft leads to hole formation. Addressing this pathway biochemically faces several obstacles, not the least of which is the difficulty in obtaining biochemically useful amounts of holin protein because of the intrinsic lethality of holins to *E. coli* (and to yeast and mammalian cells) (21, 22). The unification of the pinholin and holin triggering pathways in terms of proceeding through raft intermediates indicates that the former may be the system of choice for systematic study on several grounds. First, the minimal functional pinholin appears to be little more than TMD2 and a short cytoplasmic domain, comprising no more than an ~35-residue polypeptide; at this size, chemical synthesis could yield sufficient protein for biophysical and structural study. Second, many features of the pinhole product, including the number of TMDs (7), the orientation with respect to the lipid and lumen, and the intermolecular contact

Table 1. FRAP data analysis

GFP fusions*	Parameters†	Mobile fraction‡	$t_{1/2}$ (s)§
S^{21}68-GFP	t = 120 s, n = 13	0.35	45.95
	t = 320 s, n = 11	0.47	69.40
S^{21}68-GFP + irsS^{21}68	t = 60 s, n = 24	0.93	12.25
	t = 180 s, n = 14	1.03	14.51
irsS^{21}68-GFP	t = 30 s, n = 22	0.97	5.77
	t = 180 s, n = 10	0.88	8.07
irsS^{21}68-GFP with DNP	t = 30 s, n = 17	0.87	3.69

*Fusions expressed in each experiment.
†Experimental parameters. t, duration of the FRAP experiment in seconds; n, number of individual cells photobleached.
‡The fraction of protein assessed as mobile based on the plateau of the FRAP recovery curve.
§The half-life of fluorescence recovery calculated from the FRAP recovery curves (details in *Experimental Procedures*).

surfaces, are reasonably well-established, even in the absence of crystallographic information (4, 7). Similarly, important features of the mobile, pretriggering homodimer intermediate have also been elucidated (15). The simplicity of this system should lend itself not only to reconstruction of the triggering process in a system where the energization of the bilayer can be controlled, such as lipid bilayer membranes (23), but also course-grained modeling, which has been increasingly useful in analysis of protein–lipid interaction systems that would otherwise be intractable to molecular study (24).

Experimental Procedures

Bacterial Strains and Plasmids. The bacterial strains, prophages, and plasmids used in this work are described in Table 2. Briefly, *E. coli* strain MG1655/*lacI*^{q1}*tonA*::Tn*10* (25) carrying plasmids pQ (26) and pR′S^{21}68, pS^{21}68$_{\Delta TMD1}$, or pirsS^{21}68 was used to express the gene *S^{21}68*, *S^{21}68$_{\Delta TMD1}$*, or *irsS^{21}68* individually. *S^{21}68* was defined previously; it is an allele of *S^{21}* in which the first three codons, encoding the alternate start that generates S^{21}71 (the natural phage 21 antiholin) (Fig. 1*A*), have been deleted. Plasmid pR′S^{21}68 is identical to pTP2 (13), except for the introduction of amber nonsense codons into *R^{21}* (positions Tyr39 and Tyr42), *Rz^{21}* (Gln100), and *$Rz1^{21}$* (Trp39). Plasmid pS^{21}68$_{\Delta TMD1}$ and pirsS^{21}68 were described elsewhere (4). The same *E. coli* strain carrying pQ and plasmids pS^{21}68-GFP, pS^{21}68$_{\Delta TMD1}$-GFP, or pirsS^{21}68-GFP were used for expression of proteins S^{21}68-GFP, S^{21}68$_{\Delta TMD1}$-GFP, or irsS^{21}68-GFP, respectively. In these strains, induction of the late gene promoter serving the lysis gene constructs is accomplished by adding isopropyl-β-D-thiogalactopyranoside (IPTG) to induce synthesis of the late activator Q. These three plasmids were constructs derived from plasmids pR′S^{21}68, pS^{21}68$_{\Delta TMD1}$, and pirsS^{21}68, respectively, with codons encoding residues Pro and Gly (CCCGGG) followed by the *gfp* gene inserted before the stop codon (UAA). The *gfp* gene in all constructs carries the monomerization mutation A206K (27) and in all fusions, lacks its Met1 (AUG) codon.

For comparison of the localization of S^{21}68-GFP in the absence or presence of irsS^{21}68, the plasmid pRE (13) or pirsS^{21}68 was transformed into the lysogen MDS12*ΔtonA*[λ*cam*(*S68-GFP R_{am}RzRz1*)^{21}] individually. This lysogen was obtained by lysogenizing *E. coli* MDS12*ΔtonA* with the phage λ*cam*(*S68-gfp R_{am}RzRz1*)^{21} (4). Phage λ*cam*(*S68-gfp R_{am}RzRz1*)^{21} was isolated from clear plaques formed by a lysate of *E. coli* MDS12*tonA::Tn10*[λ*camΔ*(*SR*)] carrying plasmid pS68-GFP(R_{am}RzRz1)^{21} on a lawn of the amber suppressor *E. coli* strain LE392 *tonA*::Tn*10* (28). Plasmid pS^{21}68-GFP (R_{am}RzRz1)^{21} is identical to pS^{21}68-GFP, except that the *Rz^{21}*and *$Rz1^{21}$* genes are WT. The lysate was obtained by passing the induced culture through a French pressure cell (Spectronic Instruments) at 16,000 psi. Chloroform was added to the lysate at a final level of 1%. Whole cells and cell debris were removed by centrifugation in a clinical centrifuge for 15 min at 4 °C.

Media, Culture Growth, and General DNA Manipulation. Cultures were grown in standard LB supplemented with antibiotics where needed: kanamycin (40 μg/mL), ampicillin (100 μg/mL), and chloramphenicol (10 μg/mL). Plasmid pQ was induced by 1 mM IPTG and 0.2% arabinose. Plasmids carried by lysogens were induced by shifting the culture from 30 °C to 42 °C for 15 min. Lysis profiles were obtained by monitoring A_{550} after thermal or IPTG/arabinose inductions as described previously (29, 30). DNP was added into each culture to a 2 mM final concentration whenever indicated. Site-directed mutagenesis, cloning steps, and DNA sequencing have been described elsewhere (29).

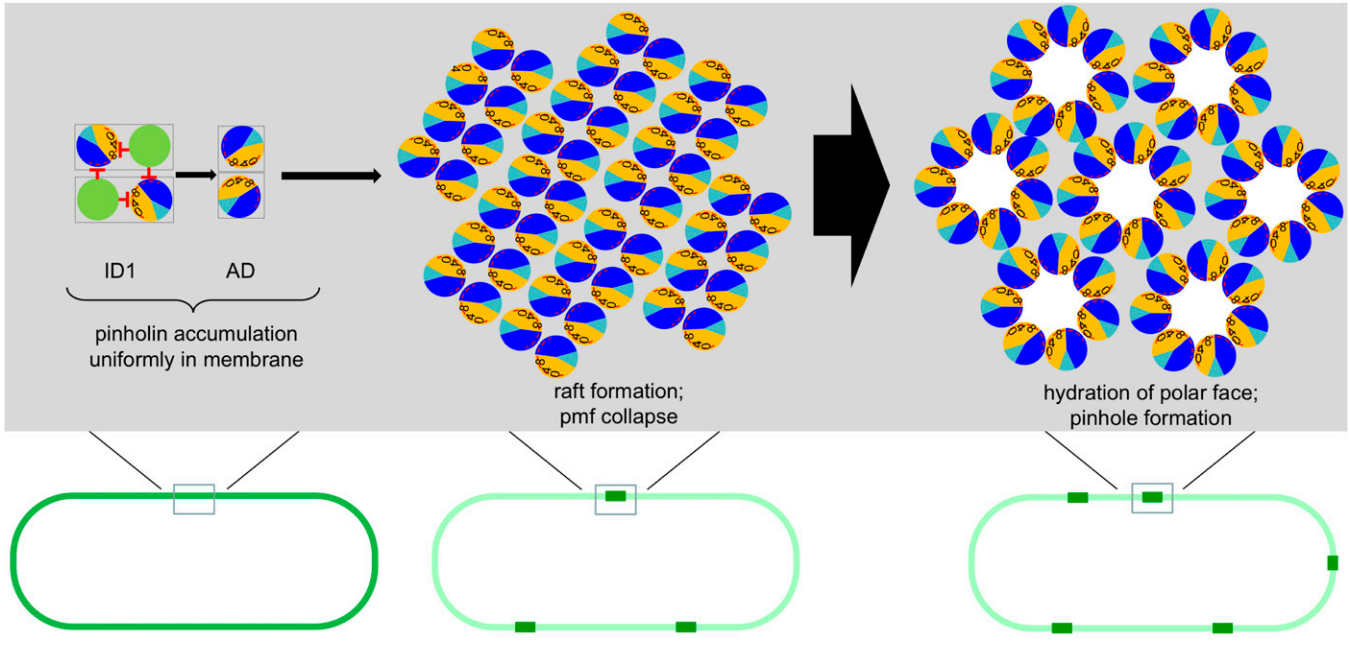

Fig. 7. Model for the pinhole formation pathway. A top-down view of a region of the cytoplasmic membrane is shown; each circle represents a helical TMD. Modified from Pang et al. (15). Fig. 1*D* defines the symbols. At a critical concentration of the AD, raft formation is nucleated. This nucleation causes a local collapse of the PMF, which in turn, leads to conformational changes in the pinholin such that the hydrophilic surfaces become hydrated and the heptameric pinholes form within the raft.

Table 2. Strains, phage, and plasmids

	Genotype and relevant features	Source
Phages		
λ*cam*Δ(*SR*)	λb_{515} b_{519} *att*::Tn*903 cI857 nin5* Δ(*SR*) *bor*::cam^r	Laboratory stock
λ*cam*(*S68-gfp* R_{am}*RzRz1*)^{21}	λ*b515 b519 att*::Tn*903 cI857 nin5* Δ(*SRRzRz1*):: (*S68-gfp* R_{am}*RzRz1*)^{21} *bor*::cam^r	This study
E. coli strains (all K–12)		
MG1655	*ilvG rfb50 rph1*	25
MG1655*lacI*^{q1} *tonA*::Tn*10*		13
MDS12	MG1655 with 12 deletions, totaling 376,180 nt, including all cryptic prophages	36
MDS12 Δ*tonA*		4
MDS12 *tonA::Tn10*		30
MDS12 *tonA::Tn10*[λ*cam*Δ(*SR*)]	Lysogen carrying prophage λ*cam*Δ(*SR*)	This study
MDS12Δ*tonA*[λ*cam*(*S68-gfp* R_{am}*RzRz1*)^{21}]	Lysogen carrying prophage λ*cam*(*S68-gfp* R_{am}*RzRz1*)^{21}	This study
MDS12Δ*tonA*(λS^{21}*68*)	Lysogen carrying prophage λS^{21}*68*	This study
LE392 *tonA*::Tn*10*	*hsdR574*($r_K^-m_K^+$) *supE44 supF58* Δ(*lacIZY*)*6 galK2 galT22 metB1 trpR55 tonA*::Tn*10*	28
Plasmids		
pTP2	pBR322 origin, pR′ promoter, *(S68/R/Rz/Rz1)*^{21}	13
pR′S^{21}68	pTP2 (R_{am}/Rz_{am}/$Rz1_{am}$)^{21}	
pS^{21}68$_{\Delta TMD1}$	pTP2 with the codons encoding TMD1 of S^{21}*68* deleted, (R_{am}/Rz_{am}/$Rz1_{am}$)^{21}	4
pirsS^{21}68	pR′S^{21}68 except encoding an S^{21}68 with the *irs* tag (residues RYIRS) fused to the N terminus	4
pQ	pSC101 origin with the λ *Q* late-activator gene under the control of the $P_{lac/ara-1}$ promoter	26
pRE	pJF118EH with *lacI*^{Q} and P_{tac} replaced by pR′ promoter	13
pGFP	pRE with *gfp* gene inserted downstream of the *pR′* promoter	Laboratory stock
pS^{21}68-GFP	pR′S^{21}68 with codons encoding linker sequence Pro and Gly (CCCGGG) and the *gfp* gene without Met1 (AUG) inserted between the last codon (GAA) of S^{21}*68* and the stop codon (UAA)	This study
pS^{21}68$_{\Delta TMD1}$-GFP	pS^{21}68$_{\Delta TMD1}$ with the linker and *gfp* same as in pS^{21}68-GFP	This study
pirsS^{21}68-GFP	pirsS^{21}68 with the linker and *gfp* same as in pS^{21}68-GFP	This study
pS^{21}68-GFP (R_{am}RzRz1)^{21}	pS^{21}68-GFP with WT $Rz^{21}$and $Rz1^{21}$	This study

Membrane Fractionation. Twenty A_{550} units of cells expressing S^{21}68-GFP or its variants were harvested at the time when S^{21}68-GFP triggered or 30 min after induction for irsS^{21}68-GFP. Pellets were resuspended in 2.5 mL buffer of 20 mM Tris (pH 7.9) and 150 mM NaCl with the addition of protease inhibitor (Sigma-Aldrich) and lysed by passing through a French pressure cell (Spectronic Instruments) at 16,000 psi. Whole cells and cell debris were removed by microcentrifugation at 10,000 × *g* for 15 min at 4 °C. Membranes were harvested by ultracentrifugation at 106,000 × *g* for 1 h at 4 °C in a Beckman TLA100.3 rotor and resuspended in 0.5 mL buffer of 20 mM Tris (pH 7.9) and 150 mM NaCl plus protease inhibitor. For SDS/PAGE and Western blotting analysis, the amounts of soluble and membrane fractions were adjusted to reflect equal volume of culture. Samples were mixed with sample loading buffer with the addition of 5% (vol/vol) β-mercaptoethanol.

Trichloroacetic Acid Precipitation, SDS/PAGE, and Western Blotting. Ten percent TCA was used to immediately stop cell growth and precipitate protein as previously described (13). Precipitates were resuspended in sample loading buffer with the addition of 5% (vol/vol) β-mercaptoethanol. SDS/PAGE and Western blotting were performed as described (4). Proteins were separated on 10% (vol/vol) Tris·Tricine gels and transferred to 0.1 μm nitrocellulose membrane (Whatman). GFP fusion protein was detected by mouse monoclonal α-GFP antibodies (Stressgen). Blots were developed by using the chromogenic substrate 4-chloro-1-naphthol (Sigma). Band intensity was determined by software ImageJ (http://rsbweb.nih.gov/ij/) (31). The amount of S^{21}68-GFP present in the induced cultures was calculated using the standard curve generated from samples containing the purified GFP protein.

Fluorescence Microscopy. Except the superresolution experiments, fluorescence microscopy was performed as described previously (32). For endpoint experiments, cultures were grown to A550 = 0.4 and induced thermally or with IPTG/arabinose; 20 μL each sample were taken out and mixed with 0.5 μL FM4-64 (1 mg/mL) at the time of pinholin triggering or 30 min after induction for irsS^{21}68-GFP, and 10 μL mixture were then put onto an agarose pad [1.2% (wt/vol) agarose, tryptone broth, 1 μg/mL FM 4-64]. Images were captured for 10 Z sections 0.2 μm apart for each sample. For samples treated with DNP, 2 mM DNP was added to each culture before collecting for microscopy study. For cells stained with DiBAC4(5), 50 μL cells were mixed with 2.5 μL 1 mg/mL DiBAC4(5)–ethanol solution and incubated at room temperature for 2 min, and 10 μL were placed on the agarose pad made without FM4-64.

For time-lapse experiments, 0.5 mL fresh overnight culture were harvested by centrifugation in a minifuge for 1 min and resuspended in 1 mL tryptone broth; 3 μL this cell suspension were placed on an agarose pad containing either 1 μg/mL FM 4-64 or 10 μg/mL DiBAC4(5). The pad was then put into a Petri dish containing wet tissues and incubated in a 37 °C incubator for 1.5 h. An inducer mixture containing 2 mM IPTG and 0.2% arabinose was placed onto each pad, and samples were observed under the microscope in the 37 °C WeatherStation environmental chamber (Precision Control). Images were taken at 1-min intervals from 5 to 34 min after induction for S^{21}68-GFP.

Images were captured by an Applied Precision optical sectioning microscope system equipped with an Olympus IX70 microscope, an Olympus Plan Apo 100× oil immersion objective (N.A. 1.4), a Photometrics Cool SNAP HQ digital camera, and Delta Vision standard fluorescence filters: FITC for GFP visualization (excitation: blue = 490/20 nm; emission: green = 528/38 nm) and RD-TR-PE for FM 4-64 and DiBAC4(5) visualization (excitation: green = 550/28 nm; emission: orange = 617/73 nm). SoftWoRx software (Applied Precision) was used to deconvolve images using the constrained iterative deconvolution algorithm. The brightness and contrast of each fluorochrome were adjusted with ImageJ (31).

Superresolution Fluorescence Microscopy. Samples were prepared in the same way as the endpoint experiments described above and imaged with the DeltaVision OMX system at the University of California at San Diego School of Medicine Light Microscopy Facility; 3D structured illumination images were acquired with a 100× 1.4 N.A. Olympus objective, 488-nm laser, and EM-CCD camera with z-stack intervals of 0.125 nm. These images were deconvolved

and aligned using SoftWoRx software to achieve an *x,y* resolution of 100 nm and *z* resolution of 250 nm.

FRAP. FRAP experiments were performed as previously described (32, 33). Sample preparation was the same as in the endpoint fluorescence microscopy experiments. After collecting a prebleach image, photobleaching was achieved using one 0.1-s pulse of a 488-nm argon laser at 50% power, and subsequent GFP images were collected at various time points at 2.5 s exposure time. The edit polygon function of the SoftWoRx software (Applied Precision) was used to define individual polygons to represent the fluorescence from the background, the whole-membrane region, and the unbleached and bleached regions of the cell. Background fluorescence was subtracted from the whole-membrane, unbleached, and bleached regions for all time points before data processing. The calculation of the corrected fraction recovery (cFR) was performed as previously described (34). For incomplete recovery, the cFR curve vs. time will plateau at a value less than one. This value indicates the fraction of the mobile GFP-tagged protein (35). The simple exponential equation [$f(t) = A(1 - \exp(-\tau \times t))$] was used to determine the curve of best fit for the average FRAP recovery curve (cFR); here, A determines the recovery fraction that the curve approaches, and τ defines the shape of the curve representing the rate of recovery. The half-life ($t_{1/2}$) was calculated using the equation ($t_{1/2} = \ln 0.5/-\tau$).

ACKNOWLEDGMENTS. This work was supported by Public Health Service Grants GM57045 (to K.P.) and GM27099 (to R.Y.). Access to the Applied Precision DeltaVision OMX microscope was provided by University of California at San Diego Neuroscience Core Grant P30 NS04710 supported by Jennifer Santini.

1. White RLY (2008) Lysis of the host by bacteriophage. *Encyclopedia of Virology*, eds Mahy BWJ, van Regenmortel MHV (Elsevier, London), Vol 3, pp 248–258.
2. Wang IN, Deaton JF, Young R (2003) Sizing the holin lesion with an endolysin-β-galactosidase fusion. *J Bacteriol* 185(3):779–787.
3. Dewey JS, et al. (2010) Micron-scale holes terminate the phage infection cycle. *Proc Natl Acad Sci USA* 107(5):2219–2223.
4. Pang T, Savva CG, Fleming KG, Struck DK, Young R (2009) Structure of the lethal phage pinhole. *Proc Natl Acad Sci USA* 106(45):18966–18971.
5. Park T, Struck DK, Dankenbring CA, Young R (2007) The pinholin of lambdoid phage 21: Control of lysis by membrane depolarization. *J Bacteriol* 189(24):9135–9139.
6. Raab R, et al. (1986) Mutational analysis of bacteriophage lambda lysis gene S. *J Bacteriol* 167(3):1035–1042.
7. Pang T, Park T, Young R (2010) Mutational analysis of the S^{21} pinholin. *Mol Microbiol* 76(1):68–77.
8. Ramanculov ER, Young R (2001) Genetic analysis of the T4 holin: Timing and topology. *Gene* 265(1-2):25–36.
9. Rydman PS, Bamford DH (2003) Identification and mutational analysis of bacteriophage PRD1 holin protein P35. *J Bacteriol* 185(13):3795–3803.
10. White R, et al. (2011) Holin triggering in real time. *Proc Natl Acad Sci USA* 108(2): 798–803.
11. Isenbarger TA, Krebs MP (1999) Role of helix-helix interactions in assembly of the bacteriorhodopsin lattice. *Biochemistry* 38(28):9023–9030.
12. Isenbarger TA, Krebs MP (2001) Thermodynamic stability of the bacteriorhodopsin lattice as measured by lipid dilution. *Biochemistry* 40(39):11923–11931.
13. Park T, Struck DK, Deaton JF, Young R (2006) Topological dynamics of holins in programmed bacterial lysis. *Proc Natl Acad Sci USA* 103(52):19713–19718.
14. Barenboim M, Chang CY, dib Hajj F, Young R (1999) Characterization of the dual start motif of a class II holin gene. *Mol Microbiol* 32(4):715–727.
15. Pang T, Park T, Young R (2010) Mapping the pinhole formation pathway of S^{21}. *Mol Microbiol* 78(3):710–719.
16. Russ WP, Engelman DM (2000) The GxxxG motif: A framework for transmembrane helix-helix association. *J Mol Biol* 296(3):911–919.
17. Kim S, et al. (2005) Transmembrane glycine zippers: Physiological and pathological roles in membrane proteins. *Proc Natl Acad Sci USA* 102(40):14278–14283.
18. Steinberg BE, Touret N, Vargas-Caballero M, Grinstein S (2007) *In situ* measurement of the electrical potential across the phagosomal membrane using FRET and its contribution to the proton-motive force. *Proc Natl Acad Sci USA* 104(22):9523–9528.
19. Wang IN, Smith DL, Young R (2000) Holins: The protein clocks of bacteriophage infections. *Annu Rev Microbiol* 54(2000):799–825.
20. Savva CG, et al. (2008) The holin of bacteriophage lambda forms rings with large diameter. *Mol Microbiol* 69(4):784–793.
21. Garrett J, Bruno C, Young R (1990) Lysis protein S of phage lambda functions in Saccharomyces cerevisiae. *J Bacteriol* 172(12):7275–7277.
22. Agu CA, et al. (2006) The cytotoxic activity of the bacteriophage lambda-holin protein reduces tumour growth rates in mammary cancer cell xenograft models. *J Gene Med* 8(2):229–241.
23. Mueller P, Rudin DO, Tien HT, Wescott WC (1962) Reconstitution of cell membrane structure in vitro and its transformation into an excitable system. *Nature* 194(1962): 979–980.
24. Khalid S, Bond PJ (2013) Multiscale molecular dynamics simulations of membrane proteins. *Methods Mol Biol* 924(2013):635–657.
25. Guyer MS, Reed RR, Steitz JA, Low KB (1981) Identification of a sex-factor-affinity site in *E. coli* as gamma delta. *Cold Spring Harb Symp Quant Biol* 45(Pt 1):135–140.
26. Gründling A, Manson MD, Young R (2001) Holins kill without warning. *Proc Natl Acad Sci USA* 98(16):9348–9352.
27. Zhang JC, Campbell RE, Ting AY, Tsien RY (2002) Creating new fluorescent probes for cell biology. *Nat Rev Mol Cell Biol* 3(12):906–918.
28. Tran TA, Struck DK, Young R (2007) The T4 RI antiholin has an N-terminal signal anchor release domain that targets it for degradation by DegP. *J Bacteriol* 189(21): 7618–7625.
29. Smith DL, Young R (1998) Oligohistidine tag mutagenesis of the lambda holin gene. *J Bacteriol* 180(16):4199–4211.
30. Tran TAT, Struck DK, Young R (2005) Periplasmic domains define holin-antiholin interactions in t4 lysis inhibition. *J Bacteriol* 187(19):6631–6640.
31. Abramoff MD, Magalhaes PJ, Ram SJ (2004) Image processing with ImageJ. *Biophotonics Int* 11(7):36–42.
32. Liu NJ, Dutton RJ, Pogliano K (2006) Evidence that the SpoIIIE DNA translocase participates in membrane fusion during cytokinesis and engulfment. *Mol Microbiol* 59(4):1097–1113.
33. Broder DH, Pogliano K (2006) Forespore engulfment mediated by a ratchet-like mechanism. *Cell* 126(5):917–928.
34. Fleming TC, et al. (2010) Dynamic SpoIIIE assembly mediates septal membrane fission during *Bacillus subtilis* sporulation. *Genes Dev* 24(11):1160–1172.
35. Wu YX, Masison DC, Eisenberg E, Greene LE (2006) Application of photobleaching for measuring diffusion of prion proteins in cytosol of yeast cells. *Methods* 39(1):43–49.
36. Kolisnychenko V, et al. (2002) Engineering a reduced *Escherichia coli* genome. *Genome Res* 12(4):640–647.